Contents lists available at ScienceDirect

Chemical Engineering Journal

journal homepage: www.elsevier.com/locate/cej

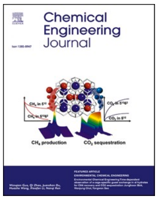

A template co-pyrolysis strategy towards the increase of amino/imino content within g-C_3N_4 for efficient CO_2 photoreduction

Ke-Ying Tao [1], Kuo Yuan [1], Wei Yang, Di-Chang Zhong [*], Tong-Bu Lu [*]

Institute for New Energy Materials and Low Carbon Technologies, School of Materials Science and Engineering, Tianjin University of Technology, Tianjin 300384, China

ARTICLE INFO

Keywords:
Template co-pyrolysis
g-C_3N_4
C–NH_x
Photocatalytic CO_2 reduction

ABSTRACT

Photocatalytic CO_2 reduction reaction (CO_2RR) is an effective mean to address the current environmental and energy issues. As a kind of typical photocatalyst, g-C_3N_4 possesses lots of advantages (i.e., facile synthesis, visible-light response, and high stability) in CO_2 reduction. However, the poor capacity of CO_2 capture and rapid recombination of photo-generated electron and hole, both hinder the further development of g-C_3N_4 for CO_2RR. Herein, we developed a template co-pyrolysis strategy to prepare C–NH_x-rich ($x = 1$ or 2) g-C_3N_4, to increase the CO_2 binding and the subsequent photocatalytic CO_2 reduction efficiency. Specifically, organic molecules with multiple imino groups were used as additives to co-pyrolyze with urea. These additives can act as templates to facilitate the formation of g-C_3N_4 with abundant C–NH_x groups, which effectively improved the capacity of CO_2 capture. Meanwhile, the capacity of light absorption and the separation of photo-generated electron and hole were also optimized. As a result, the obtained C–NH_x-rich g-C_3N_4 showed greatly enhanced photocatalytic activity for CO_2RR, over 74-fold higher than that of g-C_3N_4 conventionally prepared. This work provides a new avenue for optimizing the g-C_3N_4-based photocatalysts for CO_2RR.

1. Introduction

The solar-driven CO_2 conversion into fuels or chemicals can effectively address the global warming and energy issues, where the development of highly-effective, robust and cost-efficient catalysts is important and urgent. During the past several years, multitudinous materials have been exploited for photocatalytic CO_2 reduction reaction (CO_2RR) [1–22], among which graphitic carbon nitride (g-C_3N_4) is a competitive candidate, as it possesses lots of advantages, including facile synthesis, low cost, visible-light absorption ability, and so on [23–27]. However, the development of efficient g-C_3N_4-based photocatalysts for CO_2RR is still a big challenge, because the narrow band gap with low electron mobility causes the rapid recombination of photo-generated electron and hole [28–30]. To enhance the separation efficiency of photo-generated electron and hole, researchers have developed various strategies, including improving crystallinity [31,32], introducing defects [33–39], doping elements [40–44], constructing heterojunctions [45–50], and so on, with which the photocatalytic activity of g-C_3N_4 for CO_2RR have been improved to some extent.

Besides promoting the separation of photo-generated electron and hole, accelerating the reaction dynamics of CO_2RR can also boost the catalytic activity. It is well-known that increasing the CO_2 concentration around the catalytic centers will accelerate the reaction dynamics of CO_2RR, as the first step of which is the CO_2 capture by the catalysts [51]. The higher capacity of CO_2 adsorption, the better photocatalytic efficiency [52,53]. Therefore, strengthening the capacity of CO_2 capture to increase the local CO_2 concentration on the g-C_3N_4 surface could enhance the photocatalytic efficiency for CO_2RR. However, to our knowledge, there is hardly any reported work about improving the CO_2 adsorption ability of pristine g-C_3N_4. Considering that amino/imino groups have shown exceptional capacity of gathering CO_2 molecules in porous materials [54,55], we speculated that modification of g-C_3N_4 with amino groups can concentrate CO_2 on the g-C_3N_4 surface and thus enhance the photocatalytic efficiency for CO_2RR. Therefore, it is of great significance to find general methods to endow pristine g-C_3N_4 with rich C–NH_x groups, which is still at a blank area but seems an effective and promising mean for enhancing CO_2RR efficiency.

Herein, a template co-pyrolysis of urea and organic molecules strategy was developed to prepare C–NH_x-rich ($x = 1$ or 2) g-C_3N_4-based materials (i.e., L-C_3N_4) with enhanced photocatalytic CO_2RR activity.

---

[*] Corresponding authors.
E-mail addresses: dczhong@email.tjut.edu.cn (D.-C. Zhong), lutongbu@tjut.edu.cn (T.-B. Lu).

[1] These authors contributed equally to this work.

https://doi.org/10.1016/j.cej.2022.140630
Received 11 October 2022; Received in revised form 19 November 2022; Accepted 24 November 2022

Please cite this article as: Ke-Ying Tao, *Chemical Engineering Journal*, https://doi.org/10.1016/j.cej.2022.140630

Specifically, the organic molecule with imino groups was pre-assembled with urea through intermolecular hydrogen bonds, and then acted as a template to facilitate the formation of C–NH_x within g-C_3N_4. The enrichment of C–NH_x contributed to the CO_2 capture, thus the CO_2 reduction efficiency was remarkably enhanced in contrast to the conventionally prepared g-C_3N_4. In this strategy, the co-catalyst Co could be in situ anchored on C–NH_x-rich g-C_3N_4 by using Co complex as addictive, which tremendously improved photocatalytic CO_2RR activity. Catalytic mechanism studies revealed that the enriched C–NH_x within g-C_3N_4 could boost the thermodynamics and accelerate the dynamics of photocatalytic CO_2RR, that is, not only improve the ability of CO_2 capture, but also optimize the capacity of light absorption and the separation of photo-generated electron and hole.

2. Experimental

2.1. Materials and chemicals

All chemicals were commercially available and used without further purification. The synthetic methods of L·8$HClO_4$ and CoL were similar to the reported literatures [56,57]. The L_y (y = 1, 2, 3) were prepared through the literature methods [58–60]. The synthesis of g-C_3N_4 was based on the previous work [23]. Cobalt(II) perchlorate hexahydrate ($Co(ClO_4)_2·6H_2O$, 98%, Macklin), cobalt(II) chloride hexahydrate ($CoCl_2·6H_2O$, AR, General-Reagent), acetonitrile (CH_3CN, HPLC, Tianjin Saifurui, Science and Technology ltd). Urea (AR, Sinopharm Chemical Reagent), 2,2′-bipyridine (AR, Aladdin), triethanolamine (TEOA, AR, Aladdin), Nafion (5 wt%, in lower aliphatic alcohols, contains 15–20% water, Aldrich). Other reagents were purchased from Aladdin with analytical grade. The purity of Ar, N_2 and CO_2 was 99.999%.

2.2. Procedures

2.2.1. Preparation of g-C_3N_4

Typically, 5.0 g urea was placed in a covered crucible and heated at 600 °C for 2 h with a heating rate of 5 °C/min under air. The yellow powder was collected and washed with deionized water and ethanol for several times, and then dried under vacuum at 60 °C for 24 h.

2.2.2. Preparation of m-L-C_3N_4

The mixture of L·8$HClO_4$ (3, 6, 12.5, 18 or 25 μmol) and urea (5.0 g) was dissolved in deionized water, which was heated to get the concentrated solution, and then the residual water was evaporated by the rotary evaporator to get uniform powder. The uniform powder was denoted as (*m*-L+urea) (*m* = 3, 6, 12.5, 18 or 25). The powder sample was placed in a covered crucible and heated at 600 °C (5 °C/min heating rate) for 2 h under air. The pyrolytic product was washed by deionized water and ethanol for several times, and dried at 60 °C under vacuum. *m*-L-C_3N_4 were obtained as light brown powder.

2.2.3. Preparation of L_y-C_3N_4

The preparation procedure of L_y-C_3N_4 was similar to that of *m*-L-C_3N_4 by using other organic additives (7.5 mg; Table 1) instead of L·8$HClO_4$.

2.2.4. Preparation of n-CoL-C_3N_4

The preparation procedure of *n*-CoL-C_3N_4 (*n* = 3, 5, 8, 12.5, 18, and 25) was similar to that of *m*-L-C_3N_4 except using CoL (3, 5, 8, 12.5, 18, or 25 μmol) instead of L·8$HClO_4$.

2.2.5. Preparation of Co-C_3N_4

The preparation procedure of Co-C_3N_4 was similar to that of 12.5-CoL-C_3N_4 except using $CoCl_2·6H_2O$ (25 μmol) instead of CoL.

2.2.6. Preparation of L-urea co-crystal

100 μL H_2O containing 0.05 mmol (3 mg) urea was dropwise added to 3 mL mixed solvent of $MeOH/CH_2Cl_2$ (*v:v* = 2:1) containing 0.004 mmol (6 mg) L·8$HClO_4$, which was transferred and sealed in a 10 mL volatile bottle, and heated at 80 °C for 24 h. This solution was allowed to stand at room temperature for a week, leading to the formation of colourless block crystals with formula of L·2urea·6H_2O·5$HClO_4$, determined by single-crystal X-ray diffraction.

Table 1
The as-synthesized samples and corresponding organic additives.

Sample L_y	Molecular formula	Molecular structures
L-C_3N_4	$C_{36}N_8H_{54}$ (L)	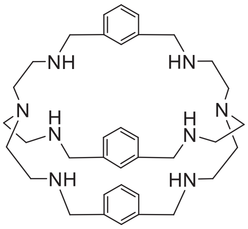
L_1-C_3N_4	$C_{27}N_4H_{36}$ (L_1)	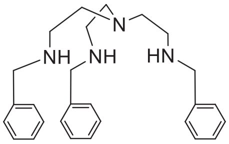
L_2-C_3N_4	$C_{18}N_4H_{18}$ (L_2)	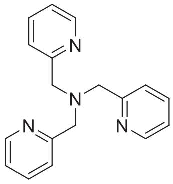
L_3-C_3N_4	$C_{17}N_3H_{15}$ (L_3)	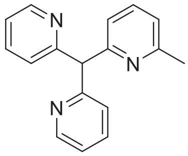

2.2.7. Preparation of L+urea

3 mg urea and 6 mg L·8$HClO_4$ were dissolved in 3.1 mL $MeOH/CH_2Cl_2/H_2O$ (*v:v:v:* = 2:1:0.1) mixed solvent. After evaporating the solvent, L+urea mixture was obtained.

2.2.8. Preparation of L_y+urea

3 mg urea and 2.5 mg L_y (*y* = 1, 2, 3) were dissolved in 3.1 mL $MeOH/CH_2Cl_2/H_2O$ (*v:v:v:* = 2:1:0.1) mixed solvent. After evaporating the solvent, L_y+urea was obtained.

2.2.9. CO_2 capture measurements in aqueous solution

First of all, the deionized water was refilled by Ar for removing dissolved CO_2. Then, 10 mg g-C_3N_4 and 12.5-L-C_3N_4 was respectively dispersed in 10 mL deionized water, and 10 mL pure deionized water was used as a reference. Due to the correlation between pH values and CO_2 concentration of aqueous solution, the CO_2 capturing amount could be determined by the pH values. By bubbling with 10 % CO_2 (Ar as balance gas; 6 sccm) into the aqueous solution, the time-dependent pH value change was detected by the pH meter at 30 °C.

2.2.10. Photoelectrochemical measurements

The photoelectrochemical measurements were monitored by using an electrochemical workstation (CHI760E) with a standard three-electrode system. The prepared FTO coated by catalyst, the Ag/AgCl (saturated KCl) electrode and a Pt plate acted as the working, reference and counter electrode, respectively. The working electrode was prepared as follows: FTO glasses were cleaned via ultrasonication in distilled water and absolute ethanol for 3 times sequentially. 5 mg catalyst powder was dispersed in 1 mL ethanol/H_2O (*v*/*v* = 3/1) mixture containing 10 μL Nafion solution (5 wt% in water). After ultrasonic treatment for 30 min, a homogeneous ink generated. The ink was dropped on the FTO (1 cm × 2 cm) with 0.5 mg/cm^2 catalyst loading. The prepared catalyst film on FTO was dried at room temperature for 10 h. 0.5 M Na_2SO_4 solution (pH = 6.8) was used as the electrolyte. Before the test, the N_2 or CO_2 was purged into the Na_2SO_4 aqueous solution for 30 min. According to the Nernst equation ($E_{RHE} = E + E_{Ag/AgCl} + 0.0591 \times pH$), the potentials versus Ag/AgCl were converted to those versus RHE (reversible hydrogen electrode). The photocurrent responses were measured under a 300 W Xe lamp at the intermittent irradiation model. Electrochemical impedance spectra (EIS) were recorded over a frequency range from 1 to 10^5 Hz.

2.2.11. Photocatalytic CO_2RR

The photocatalytic CO_2 reduction experiments were operated in a quartz tube (17 mL) containing 3 mg photocatalysts (For m-L-C_3N_4 and L_y-C_3N_4, 0.57 μmol $CoCl_2$ was added as a co-catalyst. The amount of $CoCl_2$ (0.57 μmol) equates to the Co amount in 3 mg 12.5-CoL-C_3N_4), 15 mg 2,2′-bipyridine, TEOA (0.3 M), and 5 mL CH_3CN/H_2O (v/v = 4:1). A 300 W Xe lamp with a 420 nm cut-off filter was used as a light source. Prior to irradiation, the reaction system was purged with CO_2 for 20 min under stirring. The reaction temperature was maintained at 25 °C by water bath under vigorous stirring. The gaseous products were analyzed by a gas chromatography.

2.3. Physical and chemical characterization

The powder X-ray diffraction (PXRD) results were obtained by using the Smart X-ray diffractometer (SmartLab 9 KW, Rigaku, Japan) with Cu Kα radiation (λ = 1.54178 Å). The content of Co in catalysts were measured by the inductively coupled plasma mass spectrometer (ICP-MS, ICAP-RQ, Thermo Fisher Scientific, Germany). Crystallographic data of L-urea co-crystal was collected by using a Rigaku CCD diffractometer with Cu-Kα radiation (λ = 1.54184 Å) at 293 K. Data processing was performed by the crystal-clear software package (Rigaku, 2015). The deposition number was CCDC 2176894. The transmission electron microscopy (TEM) measurements were operated on a Transmission Electron Microscope with a LaB_6 Gun (TeC3N4ai G2 spirit TWIN, FEI, USA) at an acceleration voltage of 120 kV. The High-Resolution Transmission Electron Microscope (HRTEM) images and the corresponding energy-dispersive X-ray spectroscopy (EDS) elemental mappings were characterized by a High-Resolution Transmission Electron (Talos F200X, FEI, USA). The HAADF-STEM images were obtained from a transmission electron microscope with a probe corrector (Titan Themis Cubed G2 60–300, FEI). Fourier transform IR (FT-IR) spectra were recorded on a PerkinElmer Frontier. The ultraviolet–visible (UV–vis) absorption spectra (UV–vis) were acquired on a UV–vis spectrophotometer (Lambda 750 UV/VIS/NIR, Perkin Elmer, USA). The CO_2 adsorption isotherm tests were performed on a multi-station specific surface micropore and vapor adsorption analyzer (BELSORP-Mas, MicrotracBEL, Japan). The photoluminescence (PL) spectra were collected by using a Hitachi F-7000 Fluorescence spectrophotometer under excitation at 367 nm. The electron paramagnetic resonance (EPR) spectroscopy was operated on an EPR spectrometer (EXMplus6-1, Bruker, Germany). The time-resolved fluorescence (TRF) measurements (excitation wavelength: 450 nm, detection wavelength: 520 nm) were tested by the FLS-1000 steady state and transient state fluorescence spectrometer (Edinburgh Instruments ltd). X-ray photoelectron spectroscopy (XPS) spectra were obtained on photoelectron spectroscopy (ESCALAB250Xi, THERMO SCIENTIFIC, United Kingdom) and calibrated versus C 1 s binding energy (284.8 eV). The gaseous products were analyzed by a gas chromatography (GC-2014 + ATF, 230C, Shimadzu, Japan), in which the thermal conductivity detector (TCD) detected H_2 and flame ionization detector (FID) was employed to measure CO and CH_4. Argon was used as carrier gas.

3. Results and discussion

3.1. Preparation and characterization of C–NH_x-rich g-C_3N_4

A cryptand ligand (L) (L = $N[(CH_2)_2NHCH_2(m\text{-}C_6H_4)CH_2NH(CH_2)_2]_3N$) with six imino groups was synthesized and tentatively selected as an organic additive to synthesize C–NH_x-rich g-C_3N_4 by co-pyrolysis with 5.0 g urea (See the Procedures; Scheme 1 and Fig. S1). Using different amounts of L (3, 6, 12.5, 18, and 25 μmol), a series of g-C_3N_4-based materials named m-L-C_3N_4 (m = 3, 6, 12.5, 18, and 25) were prepared. Transmission electron microscopy (TEM) images show that m-L-C_3N_4 possess similar nanosheet morphology as g-C_3N_4 (Fig. 1a and S2). Powder X-ray diffraction (PXRD) patterns reveal that m-L-C_3N_4 have the same crystal structures as conventionally prepared g-C_3N_4 (i.e., g-C_3N_4, see the Procedures; Fig. 1b). Elemental analysis results demonstrate that the content of C and N in m-L-C_3N_4 are also similar to those in g-C_3N_4 (Table S1, Entry 1–6). To further analyze the chemical configurations and stoichiometric compositions of as-synthesized samples, X-ray photoelectron spectroscopy (XPS) were employed. The C 1 s XPS profiles of g-C_3N_4 and m-L-C_3N_4 show three kinds of characteristic peaks at ~284.7, ~286.0, and ~288.2 eV, corresponding to sp^3 C—C, C–NH_x, and sp^2 N–C=N, respectively (Fig. 1c and Fig. S3) [41]. The decreased intensity of sp^2 N–C=N peak reveals the defects within L-C_3N_4. The N 1 s XPS spectra of g-C_3N_4 and m-L-C_3N_4 display-three characteristic peaks at ~398.6, ~400.0 and ~401.0 eV, assigning to C=N–C, N–$(C)_3$, and C–NH_x groups, respectively (Fig. 1d and Fig. S4) [35]. It should be noted that the percentage of C–NH_x in m-L-C_3N_4 is obviously higher than that of g-C_3N_4 based on the analysis of XPS results (Fig. S5; Table S2, Entry 1–6). When L amount increases from 3 to 12.5 μmol, the percentage of C–NH_x in m-L-C_3N_4 gradually enhances. With the further increase of L amount, the percentage of C–NH_x slightly decreases. 12.5-L-C_3N_4 possesses the highest C–NH_x content (19.4 %), much higher than g-C_3N_4 (10.8 %).

3.2. Templated Co-pyrolysis strategy

It is interesting to find that the introduction of organic additive L to the pyrolysis process of urea afforded g-C_3N_4 materials with enhanced C–NH_x content. For revealing the regulating effect of organic additives on the formation of C–NH_x in g-C_3N_4, three other organic molecules containing imino N or pyridine N atoms were employed as additives in g-C_3N_4 preparation process (Table 1). Three kinds of g-C_3N_4-based materials, i.e., L_y-C_3N_4 (y = 1, 2, 3; Table 1; Fig. S6-S8), were thus obtained. PXRD results show that all the as-synthesized L_y-C_3N_4 keep the same crystal structures as g-C_3N_4 (Fig. S9). As shown in Fig. S10, the TEM images show that L_y-C_3N_4 possess similar lamellar structures as g-C_3N_4. XPS and elemental analysis results show that the organic additive L_1 with three imino groups plays the similar role as L; the introduction of L_1 to the pyrolysis process of urea can also effectively increase the percentage of C–NH_x in obtained L_1-C_3N_4 (Fig. S11-S13; Table S2, Entry 7–9). For L_2 and L_3 containing pyridine N atoms, the C–NH_x-rich g-C_3N_4 based samples can also be obtained, but not as effective as L and L_1 with multiple imino groups. These results indicate that the imino groups of the organic additives contribute to obtain L_y-C_3N_4 with high C–NH_x content.

On the basis of elemental analysis and XPS results, the N amount of added organic additives and the increased N amount of C–NH_x in obtained m-L-C_3N_4 and L_y-C_3N_4 over that of g-C_3N_4 were further quantitatively calculated (Fig. 1e; Table S2, Entry 1–9). It is clearly seen that the increased N amount of C–NH_x in m-L-C_3N_4 is much higher than the N amount of added L (Fig. 1e), and similar phenomena also occured in L_y-C_3N_4 samples (Fig. 1f). Based on these result, not only did the imino groups in these organic additives participate in the urea polymerization process and transfer to the resulted m-L-C_3N_4 and L_y-C_3N_4, but also organic additives could induce the N of part urea to form C–NH_x rather than tri-s-triazine N.

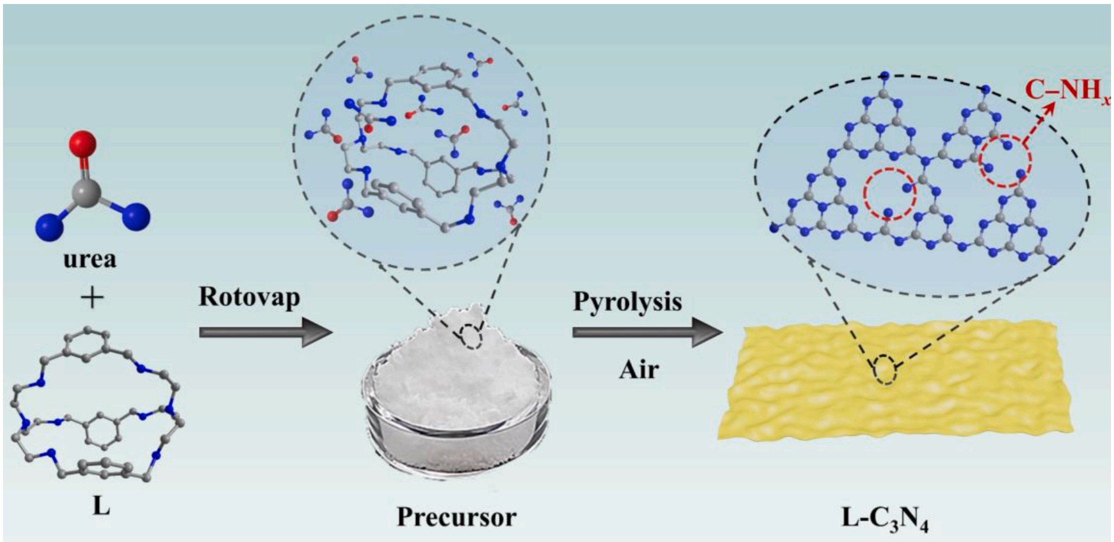

Scheme 1. Schematic process of the co-pyrolysis of L and urea to prepare C–NH$_x$-rich g-C$_3$N$_4$ (i.e., L-C$_3$N$_4$).

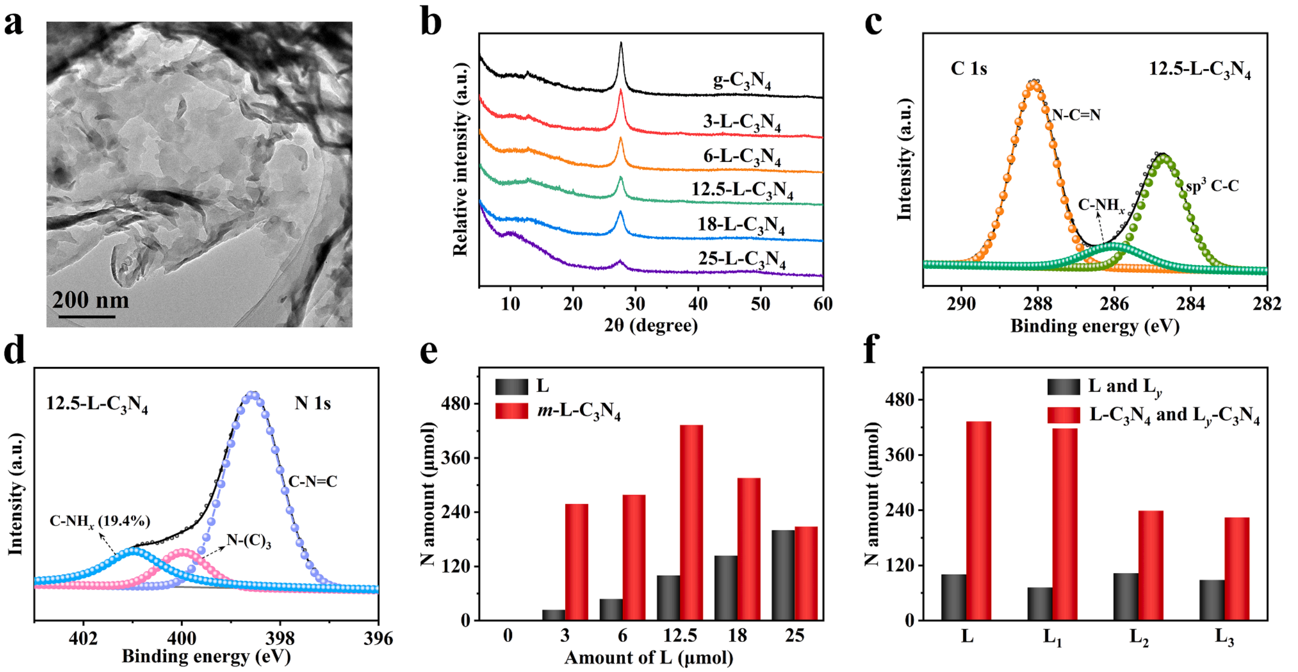

Fig. 1. (a) TEM image of 12.5-L-C$_3$N$_4$. (b) PXRD patterns of m-L-C$_3$N$_4$ (m = 3, 6, 12.5, 18, and 25) and g-C$_3$N$_4$ conventionally prepared. (c) C 1 s and (d) N 1 s XPS spectra of 12.5-L-C$_3$N$_4$. (e) The N amount in added L (black) and the increased N amount of C–NH$_x$ in m-L-C$_3$N$_4$ (red) over that of g-C$_3$N$_4$. (f) The N amount in added L and L$_y$ (black), as well as the increased N amount of C–NH$_x$ (red) in 12.5-L-C$_3$N$_4$ and L$_y$-C$_3$N$_4$.

To deeply reveal the effect of organic additive L on inducing urea to form C–NH$_x$, the pre-assembled structure of L and urea has been determined by the single X-ray diffraction (See the Procedures). As shown in Fig. 2a, the asymmetric unit of the pre-assembled structure, i.e., L-urea co-crystal, contains one L molecule and two urea molecules. Two types of intermolecular N—H···O hydrogen bonds between the imino groups of L and the carbonyl groups of urea were observed, respectively possessing the N···O distances of 2.759(5) and 2.750(5) Å, and the N—H—O angels of 168° and 162° (Table S3). These distances and angles indicate the formation of strong hydrogen bonds between L and urea [61]. The hydrogen bonds were further confirmed by Fourier Transform-Infrared Spectroscopy (FT-IR) analysis. As shown in Fig. 2b, the characteristic peak of carbonyl group stretching vibration ($\nu_{C=O}$) of urea locates at 1678.0 cm^{-1}, and the corresponding characteristic peak for L-urea co-crystal is red-shifted to 1657.7 cm^{-1} [62]. The similar results are observed in the mixture of L and urea (Fig. S14-S15), illustrating the existence of hydrogen bonds in the precursor 12.5-L+urea for preparing L-C$_3$N$_4$. These hydrogen bonds might influence the behavior of carbonyl group during urea polymerization. In reported urea pyrolysis processes to prepare g-C$_3$N$_4$, urea is firstly dehydrated to form cyanamide monomers which were then polymerized into melamine ring, and the tri-s-triazine nitrogen carbide is finally obtained (Fig. S16) [63]. For revealing urea dehydration, the pure urea and 12.5-L+urea mixture were respectively heated at 250 °C for different time (5, 20 and 30 min) to simulate the intermediate state during pyrolysis process, which was characterized by the FT-IR measurements. As for the pure urea, the characteristic peak of the $\nu_{C=O}$ at 1679.0 cm^{-1} gradually broadens and passivates with the extension of the pyrolysis time, while for 12.5-

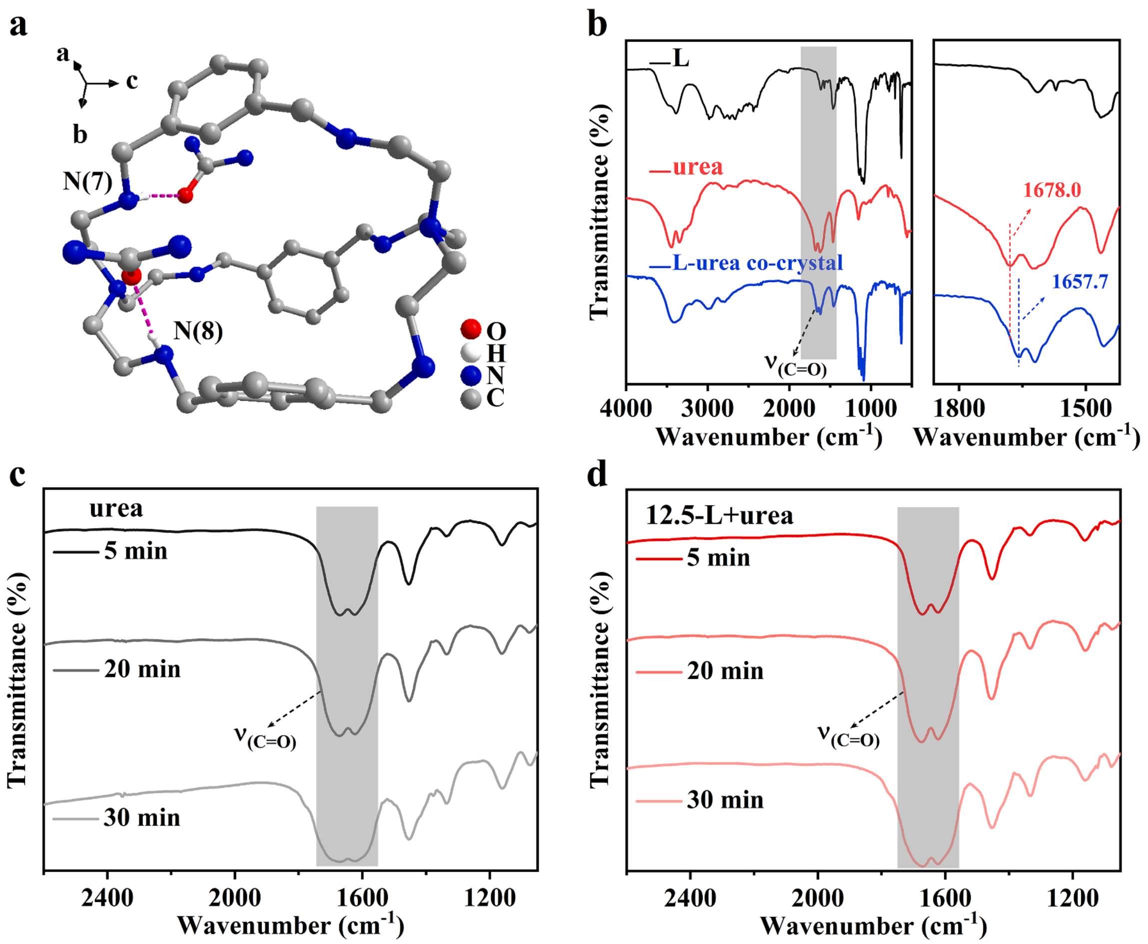

Fig. 2. (a) Crystal structure of L-urea co-crystal. (b) FT-IR spectra of L, urea and L-urea co-crystal. FT-IR spectra of (c) urea and (d) 12.5-L+urea heated at 250 °C for 5 min, 20 min and 30 min.

L+urea mixture, the $\nu_{C=O}$ characteristic peak under the same condition could be maintained to some extent (Fig. 2c, 2d). The more stable carbonyl group indicates that the hydrogen bonds between L and urea restrained the dehydration of urea in some degree. Therefore, the formation of cyanamide monomers was hindered partly, and part amino/imino groups N are formed instead of tri-s-triazine N within the as-synthesized samples. In general, the N—H···O intermolecular hydrogen bonds contribute to the pre-assemble structure of organic additive L and urea, and during the co-pyrolysis, organic additive L acts as a template to induce the N of neighboring urea to form C–NH$_x$ rather than tri-s-triazine N, which all facilitate the formation of C–NH$_x$ within the g-C_3N_4-based materials.

3.3. CO_2 adsorption capacity

With high C–NH$_x$ content in L-C_3N_4, the capacity of L-C_3N_4 to gather CO_2 molecules was measured. The CO_2 adsorption and desorption isotherms show that 12.5-L-C_3N_4 exhibits better ability of adsorbing CO_2 than g-C_3N_4 (Fig. 3a). The larger adsorption hysteresis of the sorption isotherm reveals the stronger interaction of 12.5-L-C_3N_4 to CO_2 than g-C_3N_4 [64]. The N_2 sorption isotherms demonstrate that 12.5-L-C_3N_4 and g-C_3N_4 possess similar specific surface area and pore structure, which further signifies that the enhancement of CO_2 adsorption is ascribed to the enriched C–NH$_x$ groups in 12.5-L-C_3N_4 (Fig. S17). Moreover, the gathering CO_2 capacity of C–NH$_x$ groups in 12.5-L-C_3N_4 in aqueous solution was further investigated (See the Procedures). The pH values of aqueous solution were correlated with the adsorbed CO_2 amount and hence were used to evaluate the CO_2 capture ability. The aqueous solution containing the same amount g-C_3N_4 or 12.5-L-C_3N_4 was bubbled with 10 % CO_2 for a certain time, and the real-time pH value was detected by the pH meter. As shown in Fig. 3b and Table S4, the initial pH values of water, g-C_3N_4 and 12.5-L-C_3N_4 aqueous solutions are respectively 6.30, 6.79 and 7.30 which are positively correlated with the C–NH$_x$ content in the solution (pure water < g-C_3N_4 < 12.5-CoL-C_3N_4). According to the real-time pH values, the corresponding ΔpH values (ΔpH = Initial pH - Final pH) were calculated to evaluate the ability of CO_2 capture (Table S4). As expected, the aqueous solution containing 12.5-L-C_3N_4 exhibits the maximum ΔpH value and the shortest pH balancing time ($t_{1/2}$), which illustrates the 12.5-L-C_3N_4 is better at gathering CO_2 than g-C_3N_4 in aqueous solution.

3.4. Performance on photocatalytic CO_2RR

Encouraged by the strong CO_2 capture capacity, the photocatalytic CO_2 reduction of *m*-L-C_3N_4 and L$_y$-C_3N_4, as well as g-C_3N_4 were exopred, with the $CoCl_2$ as a co-catalyst (designated as *m*-L-C_3N_4&$CoCl_2$). As expected, both *m*-L-C_3N_4 and L$_y$-C_3N_4, containing higher C–NH$_x$ content than g-C_3N_4, possess markedly enhanced photocatalytic activity for CO_2 reduction (Fig. 3c, 3d). Moreover, the activity enhancement is closely related with the C–NH$_x$ content. The more C–NH$_x$ groups, the higher photocatalytic CO_2RR activity. For *m*-L-C_3N_4, 12.5-L-C_3N_4 has the highest C–NH$_x$ content, thus displays the best photocatalytic activity, with the CO yield of 185.7 μmol·g^{-1}·h^{-1}, over 74-fold higher than that of g-C_3N_4 (2.5 μmol·g^{-1}·h^{-1}; Fig. 3c). For L$_y$-C_3N_4, L$_1$-C_3N_4 has similar C–NH$_x$ content to L-C_3N_4 (12.5-L-C_3N_4), thus displays similar photocatalytic activity. Both of them are higher than those of L$_3$-C_3N_4 and L$_4$-

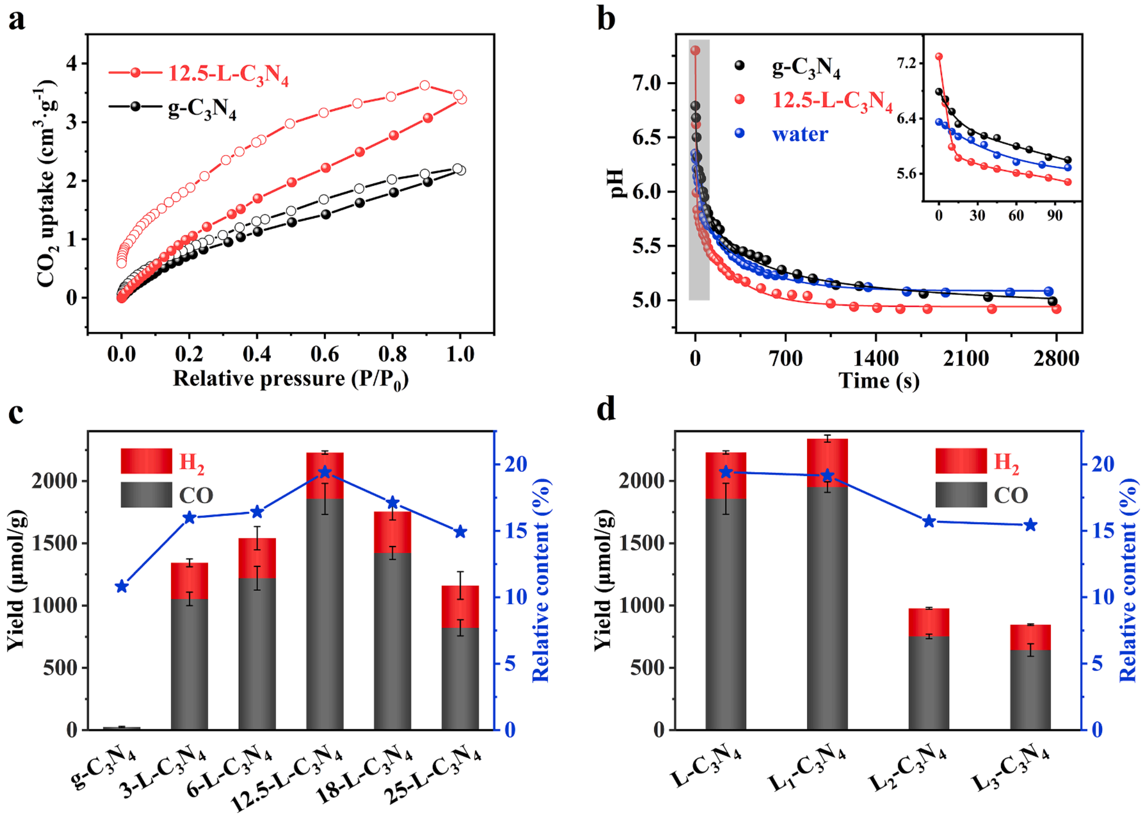

Fig. 3. (a) CO_2 adsorption and desorption isotherms of 12.5-L-C_3N_4 and g-C_3N_4 at 298 K. (b) The real-time pH values of aqueous solution containing 12.5-L-C_3N_4, g-C_3N_4, and pure water with the CO_2 bubbling. The catalytic performance and different C–NH_x content of (c) *m*-L-C_3N_4 and (d) L_y-C_3N_4. Conditions: 3 mg photocatalysts, $CoCl_2$ (0.57 μmol), TEOA (0.3 M), 15 mg 2,2′-bipyridine, 5 mL CH_3CN/H_2O (v/v = 4:1), 300 W Xe lamp (λ > 420 nm), 10 h, 25 °C.

C_3N_4 with lower C–NH_x content (Fig. 3d). The above results clearly elucidate that the rich C–NH_x groups within g-C_3N_4 greatly contribute to the enhancement of the photocatalytic CO_2 reduction activity.

In the above photocatalytic CO_2RR, the $CoCl_2$ as a co-catalyst was dissolved in reaction solution, which may be unfavorable for the electron transfer from C–NH_x-rich g-C_3N_4 to Co(II) sites. In the template co-pyrolysis strategy, the organic addictive CoL containing Co co-catalyst, which confined and facilitated Co sites in situ anchored on C–NH_x-rich g-C_3N_4 (i.e., *n*-CoL-C_3N_4, *n* = 3, 5, 8, 12.5, 18, and 25; See the Supporting Information; Fig. S18 and Table S5). In addition, the Co-decorated g-C_3N_4 (Co-C_3N_4) as a reference was synthesized by using $CoCl_2·6H_2O$ instead of CoL. The PXRD and TEM images show that there are no Co nanoparticles (Fig. S19-S20). The high-angle annular dark-field scanning transmission electron images demonstrate that scattered bright dots marked by green circles are highly dispersed, further confirming the existence of the distributed single Co atoms (Fig. 4a, 4b). EDS elemental mapping shows that the Co, C, N are uniformly dispersed (Fig. S21). The X-ray absorption fine structure (XAFS) spectroscopy results further exhibit that single-atom Co sites (valence state close to + 2) via Co-N coordination bonds are uniformly dispersed on g-C_3N_4-based nanosheets (Fig. 4c, 4d and S22-S24). According to the XPS results and elementary analysis, the distribution of different N functionalities in 12.5-CoL-C_3N_4 is similar to 12.5-L-C_3N_4, and that in Co-C_3N_4 is similar to g-C_3N_4, which means 12.5-CoL-C_3N_4 possesses higher C–NH_x content than Co-C_3N_4 and g-C_3N_4 (Fig. S25-S26; Table S1, Entry 11–12). The enrichment of C–NH_x in 12.5-L-C_3N_4 was further confirmed by gas sorption tests. The results show that 12.5-CoL-C_3N_4 and Co-C_3N_4 display similar N_2 sorption isotherms at 77 K (Fig. S27), while exhibits markedly higher CO_2 uptake than Co-C_3N_4 at 298 K (Fig. S28), which can be ascribed to the increased C–NH_x content contributing to the CO_2 capture.

The photocatalytic activity of *n*-CoL-C_3N_4 for CO_2 reduction was evaluated under the same conditions used above (Fig. S29). As expected, all *n*-CoL-C_3N_4 exhibits photocatalytic activity for CO_2 reduction. The control experiments indicate that the photocatalysts, TEOA and light are all essential factors for the occurrence of CO_2 reduction reaction (Table S6). The $^{13}CO_2$ isotope trace experiments show that ^{13}CO was detected, illustrating that the CO originated from the CO_2 reduction (Fig. S30). Furthermore, among all tested photocatalysts, 12.5-CoL-C_3N_4 exhibits the highest photocatalytic activity, with the CO yield of 263.5 $μmol·g^{-1}·h^{-1}$, higher than that of 12.5-L-C_3N_4&$CoCl_2$ (185.7 $μmol·g^{-1}·h^{-1}$, discussed above). The result elucidates that the anchoring of Co(II) on the surface of g-C_3N_4 can really accelerate the electron transfer, and thus further boosts the photocatalytic CO_2 reduction activity [65]. Moreover, the results of photocatalytic CO_2 reduction show that the CO yield of 12.5-CoL-C_3N_4 is much higher than that of Co-C_3N_4 (5.9 $μmol·g^{-1}·h^{-1}$), and the yield of 12.5-L-C_3N_4&$CoCl_2$ (185.7 $μmol·g^{-1}·h^{-1}$) is also much higher than that of g-C_3N_4&$CoCl_2$ (2.5 $μmol·g^{-1}·h^{-1}$; Fig. 5a). These results further illustrate that rich C–NH_x groups in g-C_3N_4-based materials are beneficial for improving their catalytic activity. As discussed above, C–NH_x groups in g-C_3N_4-based photocatalysts can strongly capture and gather CO_2, which would increase the local CO_2 concentration around the catalytic Co centers, and thus accelerate the catalytic reaction dynamics, greatly boosting the conversion of CO_2 to CO. In addition to the excellent photocatalytic performance, 12.5-CoL-C_3N_4 also possesses high stability; after five-cycle experiments, the catalytic activity, crystal structure and morphology of 12.5-CoL-C_3N_4 are still maintained (Fig. S31-S32). To our knowledge, 12.5-CoL-C_3N_4 as the first case of molecular-complex-derived g-C_3N_4-based photocatalyst, possesses much higher photocatalytic activity for CO_2 reduction than other reported g-C_3N_4-based composite catalysts (Table S7).

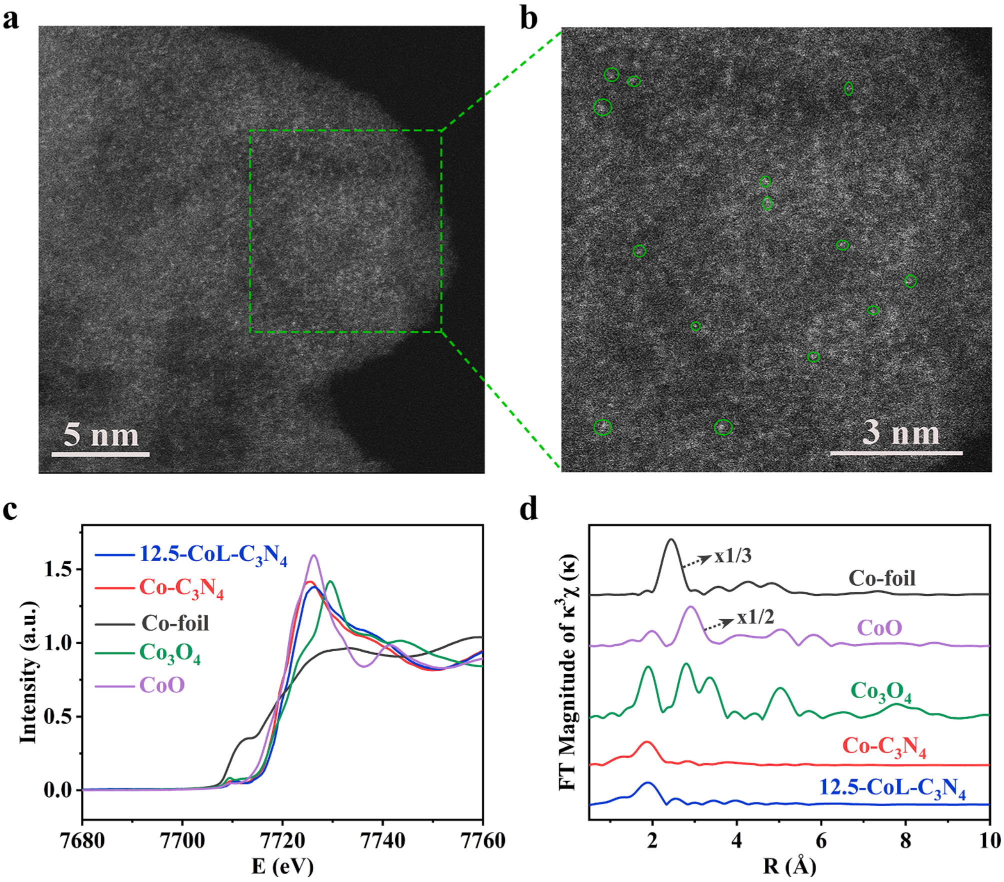

Fig. 4. (a) and (b) HAADF-STEM images of 12.5-CoL-C_3N_4. (c) Co K-edge XANES profiles and (d) Co K-edge k^3-weighted FT-EXAFS spectra of 12.5-CoL-C_3N_4, Co-C_3N_4 and the reference samples (Co foil, Co_3O_4 and CoO).

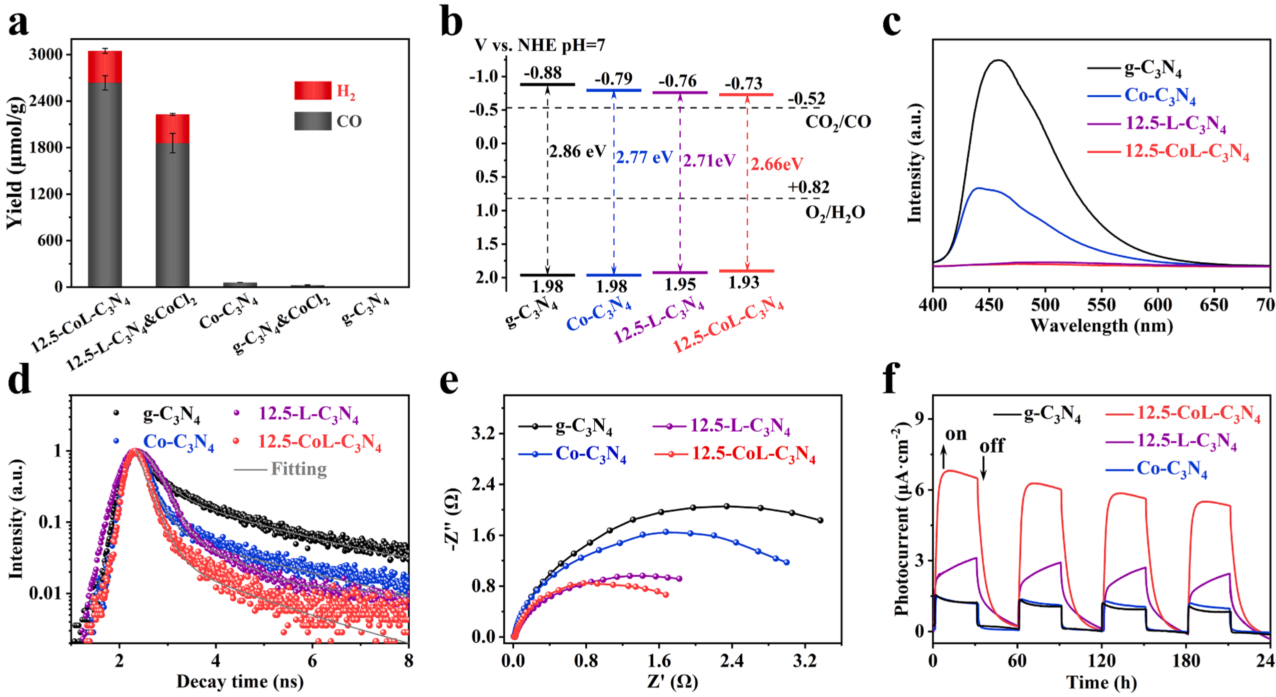

Fig. 5. (a) CO and H_2 yield over different g-C_3N_4-based catalysts under Xe lamp (300 W, λ > 420 nm) for 10 h. (b) Electronic band structures, (c) PL spectra, (d) time-resolved PL spectra, (e) electrochemical impedance spectroscopy (EIS) Nyquist plots, and (f) photocurrent responses of g-C_3N_4, Co-C_3N_4 12.5-L-C_3N_4 and 12.5-CoL-C_3N_4.

3.5. Mechanism of photocatalytic CO_2RR

The above results indicate that the increase of C–NH_x content in g-C_3N_4 is beneficial to improve the photocatalytic CO_2 reduction activity. To further reveal the effect of C–NH_x on improving photocatalytic CO_2 reduction performance, the mechanism of CO_2RR by g-C_3N_4-based photocatalysts was explored in thermodynamics and dynamics. The UV–vis absorption spectra show that the light-harvesting capability of g-C_3N_4-based photocatalysts is obviously improved in the range of $\lambda >$ 400 nm with the help of C–NH_x and/or Co implanting (Fig. S33). Thanks to the rich C–NH_x, 12.5-L-C_3N_4 possesses a narrower bandgap (Fig. S34). The conduction band potentials of photocatalysts can be roughly derived from Mott-Schottky plots (Fig. S35). Based on these, the electronic band structures of g-C_3N_4, Co-C_3N_4, 12.5-L-C_3N_4 and 12.5-CoL-C_3N_4 were schemed in Fig. 5b. The CB potentials of these samples are more negative than the redox potential of $\varphi(CO_2/CO)$ (-0.52 eV vs NHE), which means the as-synthesized catalysts are capable of photocatalyzing CO_2RR thermodynamics.

As for the dynamics of CO_2RR, the ability of CO_2 capture is one of the important aspects. The increase of C–NH_x content in g-C_3N_4-based photocatalysts contributes to capture and gather CO_2 in solid and aqueous solution, and thus benefits to the subsequent photoreduction have been discussed above in detail. Especially, the CO_2 capture in aqueous solution simulated the condition of catalytic system. 12.5-L-C_3N_4 with rich C–NH_x showed much better at CO_2 capture than g-C_3N_4, which well illustrated that the enrichment of C–NH_x within L-C_3N_4 could enhance the CO_2 concentration around catalytic sites. In addition, the separation and transport of photo-generated charge is another essential aspect. As shown in the photoluminescence (PL) spectra, the PL intensity of *m*-L-C_3N_4, L_y-C_3N_4 and 12.5-CoL-C_3N_4 is much lower than that of g-C_3N_4 (Fig. 5c and Fig. S36), which signify that C–NH_x facilitates the separation efficiency of photo-generated electron and hole. Furthermore, in the electron paramagnetic resonance (EPR) spectra, the only one single Lorent-zian line at $g = 2.003$ belongs to lone pair electrons of sp^2-carbon in the aromatic rings [31,66]. In comparison with g-C_3N_4 and Co-C_3N_4, 12.5-CoL-C_3N_4 exhibits highest EPR signal, demonstrating that with rich C–NH_x groups, there is more unpaired electrons in 12.5-CoL-C_3N_4 (Fig. S37a). Under irradiation, the intensity of peak further increased (Fig. S37b), which indicate that more free electrons are generated [67]. The average exciton lifetimes of g-C_3N_4, Co-C_3N_4, 12.5-L-C_3N_4 and 12.5-CoL-C_3N_4 are respectively 3.956, 1.759, 1.133 and 0.7437 ns, which illuminates that the electronic transfer process in 12.5-L-C_3N_4 and 12.5-CoL-C_3N_4 is faster than in g-C_3N_4 and Co-C_3N_4 (Fig. 5d and Table S8). The EIS Nyquist plots show smaller diameter of capacitive loop of 12.5-CoL-C_3N_4 and 12.5-L-C_3N_4 over Co-C_3N_4 and g-C_3N_4, also confirms the smaller charge-transfer resistance (Fig. 5e). Electrochemical measurements show that the photocurrent density of 12.5-CoL-C_3N_4 is over 6 times larger than that of Co-C_3N_4, and 12.5-L-C_3N_4 is over 3 times larger than that of g-C_3N_4, further suggests that better separation efficiency of photoinduced electrons with the help of C–NH_x (Fig. 5f). The shorter average exciton lifetime, smaller diameter of capacitive loop, as well as higher photocurrent density of 12.5-CoL-C_3N_4 and 12.5-L-C_3N_4 over Co-C_3N_4 and g-C_3N_4, all evidence the better separation efficiency of photo-generated electron and hole with the help of C–NH_x. The high percentage of C–NH_x groups not only optimize the light adsorption, but also improve the capacity of CO_2 capture and the separation of photo-generated electron and hole, all of which are in favor of boosting the photocatalytic activity of CO_2RR.

4. Conclusion

In this work, we developed a template co-pyrolysis strategy to prepare C–NH_x-rich g-C_3N_4 (L-C_3N_4). The organic addictive could form the pre-assemble structure with urea via intermolecular hydrogen bonds, and then acted as a template to facilitate the formation of C–NH_x within L-C_3N_4. The C–NH_x functionalities not only improve the ability of gathering CO_2, but also optimize the capacity of light absorption and the separation of photo-generated electron and hole, which greatly boost the photocatalytic CO_2 reduction activity. In this ingenious strategy, the single-atom co-catalyst Co can be in situ anchored on L-C_3N_4 nanosheets by employing CoL as addictive, which further enhances the photocatalytic CO_2 reduction activity. This work develops a template co-pyrolysis strategy and firstly succeeds in regulating C–NH_x content within in g-C_3N_4, which opens a novel avenue for developing highly efficient g-C_3N_4-based photocatalysts for CO_2RR.

Declaration of Competing Interest

The authors declare that they have no known competing financial interests or personal relationships that could have appeared to influence the work reported in this paper.

Data availability

Data will be made available on request.

Acknowledgements

This work was supported by the National Natural Science Foundation of China (21861001, 21931007, 22001043, 22071182), the National Key R&D Program of China (2017YFA0700104), the 111 Project of China (D17003) and the Science & Technology Development Fund of Tianjin Education Commission for Higher Education (2018KJ129).

Appendix A. Supplementary data

Supplementary data to this article can be found online at https://doi.org/10.1016/j.cej.2022.140630.

References

[1] W. Yang, H.J. Wang, R.R. Liu, J.W. Wang, C. Zhang, C. Li, D.C. Zhong, T.B. Lu, Tailoring Crystal Facets of Metal-Organic Layers to Enhance Photocatalytic Activity for CO_2 Reduction, Angew. Chem. Int. Ed. 60 (2021) 409–414.

[2] T. Ouyang, H.J. Wang, H.H. Huang, J.W. Wang, S. Guo, W.J. Liu, D.C. Zhong, T. B. Lu, Dinuclear Metal Synergistic Catalysis Boosts Photochemical CO_2-to-CO Conversion, Angew. Chem. Int. Ed. 57 (2018) 16480–16485.

[3] G. Wang, C.T. He, R. Huang, J.J. Mao, D.S. Wang, Y.D. Li, Photoinduction of Cu Single Atoms Decorated on UiO-66-NH_2 for Enhanced Photocatalytic Reduction of CO_2 to Liquid Fuels, J. Am. Chem. Soc. 142 (2020) 19339–19345.

[4] X.L. Zu, Y. Zhao, X.D. Li, R.H. Chen, W.W. Shao, Z.Q. Wang, J. Hu, J.F. Zhu, Y. Pan, Y.F. Sun, Y. Xie, Ultrastable and Efficient Visible-light-driven CO_2 Reduction Triggered by Regenerative Oxygen-Vacancies in $Bi_2O_2CO_3$ Nanosheets, Angew. Chem. Int. Ed. 60 (2021) 13840–13846.

[5] Z.K. Xin, M.Y. Huang, Y. Wang, Y.J. Gao, Q. Guo, X.B. Li, C.H. Tung, L.Z. Wu, Reductive Carbon-Carbon Coupling on Metal Sites Regulates Photocatalytic CO_2 Reduction in Water Using ZnSe Quantum Dots, Angew. Chem. Int. Ed. n/a (2022) e202207222.

[6] M. Lu, M. Zhang, J. Liu, T.Y. Yu, J.N. Chang, L.J. Shang, S.L. Li, Y.Q. Lan, Confining and Highly Dispersing Single Polyoxometalate Clusters in Covalent Organic Frameworks by Covalent Linkages for CO_2 Photoreduction, J. Am. Chem. Soc. 144 (2022) 1861–1871.

[7] J. Li, H.L. Huang, W.J. Xue, K. Sun, X.H. Song, C.R. Wu, L. Nie, Y. Li, C.Y. Liu, Y. Pan, H.L. Jiang, D.H. Mei, C.L. Zhong, Self-adaptive dual-metal-site pairs in metal-organic frameworks for selective CO_2 photoreduction to CH_4, Nat. Catal. 4 (2021) 719–729.

[8] J.W. Wang, L. Jiang, H.H. Huang, Z.J. Han, G.F. Ouyang, Rapid electron transfer via dynamic coordinative interaction boosts quantum efficiency for photocatalytic CO_2 reduction, Nat. Commun. 12 (2021) 4276.

[9] Z.H. Li, R. Shi, J.Q. Zhao, T.R. Zhang, Ni-based catalysts derived from layered-double-hydroxide nanosheets for efficient photothermal CO_2 reduction under flow-type system, Nano Res. 14 (2021) 4828–4832.

[10] L.Y. Wu, Y.F. Mu, X.X. Guo, W. Zhang, Z.M. Zhang, M. Zhang, T.B. Lu, Encapsulating Perovskite Quantum Dots in Iron-Based Metal-Organic Frameworks (MOFs) for Efficient Photocatalytic CO_2 Reduction, Angew. Chem. Int. Ed. 58 (2019) 9491–9495.

[11] T. Lv, J.X. Li, N. Arif, L. Qi, J.G. Lu, Z.Z. Ye, Y.J. Zeng, Polarization and external-field enhanced photocatalysis, Matter, (2022).

[12] T. Billo, I. Shown, A.k. Anbalagan, T.A. Effendi, A. Sabbah, F.Y. Fu, C.M. Chu, W.Y. Woon, R.S. Chen, C.H. Lee, K.H. Chen, L.C. Chen, A mechanistic study of molecular

CO_2 interaction and adsorption on carbon implanted SnS_2 thin film for photocatalytic CO_2 reduction activity, Nano Energy, 72 (2020) 104717.

[13] J. Xiong, P. Song, J. Di, H.M. Li, Ultrathin structured photocatalysts: A versatile platform for CO_2 reduction, Appl Catal B 256 (2019), 117788.

[14] H.Y. Jiang, K.-I. Katsumata, J. Hong, A. Yamaguchi, K. Nakata, C. Terashima, N. Matsushita, M. Miyauchi, A. Fujishima, Photocatalytic reduction of CO_2 on Cu_2O-loaded Zn-Cr layered double hydroxides, Appl Catal B 224 (2018) 783–790.

[15] F. Zhang, Y.H. Li, M.Y. Qi, Z.R. Tang, Y.J. Xu, Boosting the activity and stability of Ag-Cu_2O/ZnO nanorods for photocatalytic CO_2 reduction, Appl Catal B 268 (2020), 118380.

[16] S.Q. Gong, X. Teng, Y.L. Niu, X. Liu, M.Z. Xu, C. Xu, L.L. Ji, Z.F. Chen, Construction of S-scheme 0D/2D heterostructures for enhanced visible-light-driven CO_2 reduction, Appl Catal B 298 (2021), 120521.

[17] Y.H. Chen, J.K. Ye, Y.J. Chang, T.W. Liu, Y.H. Chuang, W.R. Liu, S.H. Liu, Y.C. Pu, Mechanisms behind photocatalytic CO_2 reduction by CsPbBr 3 perovskite-graphene-based nanoheterostructures, Appl Catal B 284 (2021), 119751.

[18] J. Li, B.J. Huang, Q. Guo, S. Guo, Z.K. Peng, J. Liu, Q.Y. Tian, Y.P. Yang, Q. Xu, Z. Y. Liu, B. Liu, Van der Waals heterojunction for selective visible-light-driven photocatalytic CO_2 reduction, Appl Catal B 284 (2021), 119733.

[19] S.J. Xie, Y.F. Li, B. Sheng, W.Y. Zhang, W. Wang, C.C. Chen, J.K. Li, H. Sheng, J. C. Zhao, Self-reconstruction of paddle-wheel copper-node to facilitate the photocatalytic CO_2 reduction to ethane, Appl Catal B 310 (2022), 121320.

[20] G. Wang, Z. Chen, T. Wang, D.S. Wang, J.J. Mao, P and Cu Dual Sites on Graphitic Carbon Nitride for Photocatalytic CO_2 Reduction to Hydrocarbon Fuels with High C_2H_6 Evolution, Angew. Chem. Int. Ed. 61 (2022) e202210789.

[21] J.L. Cheng, Y.F. Mu, L.Y. Wu, Z.L. Liu, K. Su, G.X. Dong, M. Zhang, T.B. Lu, Acetate-assistant efficient cation-exchange of halide perovskite nanocrystals to boost the photocatalytic CO_2 reduction, Nano Res. 15 (2022) 1845–1852.

[22] J.Z. Wang, H. Li, P. Gao, Y. Peng, S.W. Cao, M. Antonietti, CsPbBr 3 perovskite based tandem device for C_O2 photoreduction, Chem. Eng. J. 443 (2022), 136447.

[23] X.C. Wang, K. Maeda, A. Thomas, K. Takanabe, G. Xin, J.M. Carlsson, K. Domen, M. Antonietti, A metal-free polymeric photocatalyst for hydrogen production from water under visible light, Nat. Mater. 8 (2009) 76–80.

[24] Y. Zheng, L.H. Lin, B. Wang, X.C. Wang, Graphitic Carbon Nitride Polymers toward Sustainable Photoredox Catalysis, Angew. Chem. Int. Ed. 54 (2015) 12868–12884.

[25] M.S. Xu, T. Liang, M.M. Shi, H.Z. Chen, Graphene-like two-dimensional materials, Chem. Rev. 113 (2013) 3766–3798.

[26] B.C. Zhu, L.Y. Zhang, B. Cheng, J.G. Yu, First-principle calculation study of tri-s-triazine-based g-C_3N_4: A review, Appl Catal B 224 (2018) 983–999.

[27] F. Yang, X.Y. Chu, J.H. Sun, Y.H. Zhang, Z.J. Li, H.Y. Liu, L.L. Bai, Y. Qu, L.Q. Jing, Efficient singlet oxygen generation by excitonic energy transfer on ultrathin g-C_3N_4 for selective photocatalytic oxidation of methyl-phenyl-sulfide with O_2, Chin. Chem. Lett. 31 (2020) 2784–2788.

[28] W.J. Ong, L.L. Tan, Y.H. Ng, S.T. Yong, S.P. Chai, Graphitic Carbon Nitride (g-C_3N_4)-Based Photocatalysts for Artificial Photosynthesis and Environmental Remediation: Are We a Step Closer To Achieving Sustainability? Chem. Rev. 116 (2016) 7159–7329.

[29] J.W. Fu, J.G. Yu, C.J. Jiang, B. Cheng, g-C_3N_4-Based Heterostructured Photocatalysts, Adv. Energy Mater. 8 (2018).

[30] L.B. Jiang, X.Z. Yuan, Y. Pan, J. Liang, G.M. Zeng, Z.B. Wu, H. Wang, Doping of graphitic carbon nitride for photocatalysis: A reveiw, Appl Catal B 217 (2017) 388–406.

[31] H.H. Ou, L.H. Lin, Y. Zheng, P.J. Yang, Y.X. Fang, X.C. Wang, Tri-s-triazine-Based Crystalline Carbon Nitride Nanosheets for an Improved Hydrogen Evolution, Adv. Mater. 29 (2017) 1700008.

[32] F. Villalobos Luis, T. Vahdat Mohammad, M. Dakhchoune, Z. Nadizadeh, M. Mensi, E. Oveisi, D. Campi, N. Marzari, V. Agrawal Kumar, Large-scale synthesis of crystalline g-C_3N_4 nanosheets and high-temperature H_2 sieving from assembled films, Sci. Adv. 6 (2020) aay9851.

[33] Y. Xiao, G.H. Tian, W. Li, Y. Xie, B.J. Jiang, C.G. Tian, D.Y. Zhao, H.G. Fu, Molecule Self-Assembly Synthesis of Porous Few-Layer Carbon Nitride for Highly Efficient Photoredox Catalysis, J. Am. Chem. Soc. 141 (2019) 2508–2515.

[34] X. Zhang, P.J. Ma, C. Wang, L.Y. Gan, X.J. Chen, P. Zhang, Y. Wang, H. Li, L. H. Wang, X.Y. Zhou, K. Zheng, Unraveling the Dual Defect Sites in Graphite Carbon Nitride for Ultra-high Photocatalytic H_2O_2 Evolution, Energ. Environ. Sci. 830–842 (2022).

[35] H.J. Yu, R. Shi, Y.X. Zhao, T. Bian, Y.F. Zhao, C. Zhou, G.I.N. Waterhouse, L.Z. Wu, C.H. Tung, T.R. Zhang, Alkali-Assisted Synthesis of Nitrogen Deficient Graphitic Carbon Nitride with Tunable Band Structures for Efficient Visible-Light-Driven Hydrogen Evolution, Adv. Mater. 29 (2017) 1605148.

[36] V.W.-h. Lau, I. Moudrakovski, T. Botari, S. Weinberger, M.B. Mesch, V. Duppel, J. Senker, V. Blum, B.V. Lotsch, Rational design of carbon nitride photocatalysts by identification of cyanamide defects as catalytically relevant sites, Nat. Commun., 7 (2016) 12165.

[37] Z. Mo, X.W. Zhu, Z.F. Jiang, Y.H. Song, D.B. Liu, H.P. Li, X.F. Yang, Y.B. She, Y. C. Lei, S.Q. Yuan, H.M. Li, L. Song, Q.Y. Yan, H. Xu, Porous nitrogen-rich g-C_3N_4 nanotubes for efficient photocatalytic CO_2 reduction, Appl Catal B 256 (2019), 117854.

[38] C.Z. Wu, S.Y. Xue, Z.J. Qin, M. Nazari, G. Yang, S. Yue, T. Tong, H. Ghasemi, F.C. R. Hernandez, S.C. Xue, D. Zhang, H.Y. Wang, Z.M. Wang, S.Y. Pu, J.M. Bao, Making g-C_3N_4 ultra-thin nanosheets active for photocatalytic overall water splitting, Appl Catal B 282 (2021), 119557.

[39] G. Capilli, M. Costamagna, F. Sordello, C. Minero, Synthesis, characterization and photocatalytic performance of p-type carbon nitride, Appl Catal B 242 (2019) 121–131.

[40] W. Liu, L.L. Cao, W.J. Cheng, Y.J. Cao, X.K. Liu, W. Zhang, X.L. Mou, L.L. Jin, X. S. Zheng, W. Che, Q.H. Liu, T. Yao, S.Q. Wei, Single-Site Active Cobalt-Based Photocatalyst with a Long Carrier Lifetime for Spontaneous Overall Water Splitting, Angew. Chem. Int. Ed. 56 (2017) 9312–9317.

[41] L.W. Zhang, R. Long, Y.M. Zhang, D.L. Duan, Y.J. Xiong, Y.J. Zhang, Y.P. Bi, Direct Observation of Dynamic Bond Evolution in Single-Atom Pt/C_3N_4 Catalysts, Angew. Chem. Int. Ed. 59 (2020) 6224–6229.

[42] S.F. Ji, Y. Qu, T. Wang, Y.J. Chen, G.F. Wang, X. Li, J.C. Dong, Q.Y. Chen, W. Y. Zhang, Z.D. Zhang, S.Y. Liang, R. Yu, Y. Wang, D.S. Wang, Y.D. Li, Rare-Earth Single Erbium Atoms for Enhanced Photocatalytic CO_2 Reduction, Angew. Chem. Int. Ed. 59 (2020) 10651–10657.

[43] Y.Y. Zhou, L. Zhang, W.Z. Wang, Direct functionalization of methane into ethanol over copper modified polymeric carbon nitride via photocatalysis, Nat. Commun. 10 (2019) 506.

[44] C.M. Ding, C.C. Feng, Y.H. Mei, F.Y. Liu, H. Wang, M. Dupuis, C. Li, Carbon nitride embedded with transition metals for selective electrocatalytic CO_2 reduction, Appl Catal B 268 (2020), 118391.

[45] J. Su, G.D. Li, X.H. Li, J.S. Chen, 2D/2D Heterojunctions for Catalysis, Adv. Sci. 6 (2019) 1801702.

[46] M. Ou, W.G. Tu, S.M. Yin, W.N. Xing, S.Y. Wu, H.J. Wang, S.P. Wan, Q. Zhong, R. Xu, Amino-Assisted Anchoring of CsPbBr 3 Perovskite Quantum Dots on Porous g-$_C$3$_N$4 for Enhanced Photocatalytic C_O2 Reduction, Angew. Chem. Int. Ed. 57 (2018) 13570–13574.

[47] P. Zhang, D.R. Sun, A. Cho, S. Weon, S. Lee, J. Lee, J.W. Han, D.P. Kim, W. Choi, Modified carbon nitride nanozyme as bifunctional glucose oxidase-peroxidase for metal-free bioinspired cascade photocatalysis, Nat. Commun. 10 (2019) 940.

[48] J.W. Sun, J. Bian, J.D. Li, Z.Q. Zhang, Z.J. Li, Y. Qu, L.L. Bai, Z.D. Yang, L.Q. Jing, Efficiently photocatalytic conversion of CO_2 on ultrathin metal phthalocyanine/g-C_3N_4 heterojunctions by promoting charge transfer and CO_2 activation, Appl Catal B 277 (2020), 119199.

[49] H. Wang, X.Z. Yuan, H. Wang, X.H. Chen, Z.B. Wu, L.B. Jiang, W.P. Xiong, G. M. Zeng, Facile synthesis of Sb_2S_3/ultrathin g-C_3N_4 sheets heterostructures embedded with g-C_3N_4 quantum dots with enhanced NIR-light photocatalytic performance, Appl Catal B 193 (2016) 36–46.

[50] R. Yan, A. Zada, L. Sun, Z.J. Li, Z.Y. Mu, S.Y. Chen, F. Yang, J.H. Sun, L.L. Bai, Y. Qu, L.Q. Jing, Comparative study of metal oxides and phosphate modification with different mechanisms over g-C_3N_4 for visible-light photocatalytic degradation of metribuzin, Rare Met. 41 (2022) 155–165.

[51] S.N. Talapaneni, G. Singh, I.Y. Kim, K. AlBahily, A.H. Al-Muhtaseb, A.S. Karakoti, E. Tavakkoli, A. Vinu, Nanostructured Carbon Nitrides for CO_2 Capture and Conversion, Adv. Mater. 32 (2020) 1904635.

[52] R. Li, W. Zhang, K. Zhou, Metal–Organic-Framework-Based Catalysts for Photoreduction of CO_2, Adv. Mater. 30 (2018) 1705512.

[53] Z. Jiang, W. Miao, X. Zhu, G. Yang, Z. Yuan, J. Chen, X. Ji, F. Kong, B. Huang, Modifying lewis base on TiO_2 nanosheets for enhancing CO_2 adsorption and the separation of photogenerated charge carriers, Appl Catal B 256 (2019), 117881.

[54] A. Greenaway, B. Gonzalez-Santiago, P.M. Donaldson, M.D. Frogley, G. Cinque, J. Sotelo, S. Moggach, E. Shiko, S. Brandani, R.F. Howe, P.A. Wright, In site Synchrotron IR Microspectroscopy of CO_2 Adsorption on Single Crystals of the Functionalized MOF $Sc_2(BDC\text{-}NH_2)_3$, Angew. Chem. Int. Ed. 53 (2014) 13483–13487.

[55] X. Su, L. Bromberg, V. Martis, F. Simeon, A. Huq, T.A. Hatton, Postsynthetic Functionalization of Mg-MOF-74 with Tetraethylenepentamine: Structural Characterization and Enhanced CO_2 Adsorption, ACS Appl. Mater. Interfaces 9 (2017) 11299–11306.

[56] T. Ouyang, H.H. Huang, J.W. Wang, D.C. Zhong, T.B. Lu, A Dinuclear Cobalt Cryptate as a Homogeneous Photocatalyst for Highly Selective and Efficient Visible-Light Driven CO_2 Reduction to CO in CH_3CN/H_2O Solution, Angew. Chem. Int. Ed. 56 (2017) 738–743.

[57] J.M. Chen, W. Wei, X.L. Feng, T.B. Lu, CO_2 fixation and transformation by a dinuclear copper cryptate under acidic conditions, Chem. Asian J. 2 (2007) 710–719.

[58] M.A. Hossain, J.A. Liljegren, D. Powell, K. Bowman-James, Anion Binding with a Tripodal Amine, Inorg. Chem. 43 (2004) 3751–3755.

[59] B.G. Gafford, R.A. Holwerda, Oxidative synthesis of bis(μ-hydroxo)chromium(III) dimers with aromatic amine ligands. Structure, physical properties, and base hydrolysis kinetics of the bis(μ-hydroxo)bis[(tris(2-pyridylmethyl)amine) chromium(III)] ion, Inorg. Chem. 28 (1989) 60–66.

[60] M. Kodera, H. Shimakoshi, M. Nishimura, H. Okawa, S. Iijima, K. Kano, Synthesis, Characterization, and Crystal Structure of a (μ-Oxo)bis(μ-acetato)diiron(III) Complex with a Dinucleating Hexapyridine Ligand, 1,2-Bis[2-(bis(2-pyridyl) methyl)-6-pyridyl]ethane. The First Example of a Discrete (μ-Oxo)bis(μ-acetato) diiron(III) Complex with a Dinucleating Ligand, Inorg. Chem. 35 (1996) 4967–4973.

[61] C.D. Sessler, M. Rahm, S. Becker, J.M. Goldberg, F. Wang, S.J. Lippard, CF_2H, a Hydrogen Bond Donor, J. Am. Chem. Soc. 139 (2017) 9325–9332.

[62] K. Yuan, T.Q. Song, C.H. Yang, J. Guo, Q.S. Sun, Y. Zou, F. Jiao, L.J. Li, X.T. Zhang, H.L. Dong, L.Q. Li, W.P. Hu, Polymer-Assisted Space-Confined Strategy for the Foot-Scale Synthesis of Flexible Metal-Organic Framework-Based Composite Films, J. Am. Chem. Soc. 143 (2021) 17526–17534.

[63] F. Dong, Z.Y. Wang, Y.J. Sun, W.K. Ho, H.D. Zhang, Engineering the nanoarchitecture and texture of polymeric carbon nitride semiconductor for enhanced visible light photocatalytic activity, J. Colloid Interface Sci. 401 (2013) 70–79.

[64] P. Ju, L. Jiang, T.B. Lu, A Three-Dimensional Dynamic Metal-Organic Framework with Fourfold Interpenetrating Diamondoid Networks and Selective Adsorption Properties, Inorg. Chem. 54 (2015) 6291–6295.

[65] J.H. Zhang, W. Yang, M. Zhang, H.J. Wang, R. Si, D.C. Zhong, T.B. Lu, Metal-organic layers as a platform for developing single-atom catalysts for photochemical CO_2 reduction, Nano Energy 80 (2021), 105542.

[66] S.S. Li, Y.N. Peng, C. Hu, Z.H. Chen, Self-assembled synthesis of benzene-ring-grafted g-C_3N_4 nanotubes for enhanced photocatalytic H_2 evolution, Appl Catal B 279 (2020), 119401.

[67] X.J. Ye, Y.J. Cui, X.C. Wang, Ferrocene-Modified Carbon Nitride for Direct Oxidation of Benzene to Phenol with Visible Light, ChemSusChem 7 (2014) 738–742.